J. Materials, Conc. Struct. Pavements, JSCE, No. 683/V-52, 157-171, 2001 August

NUMERICAL SIMULATION OF FAILURE PATH FORMATION AND CRACK SEQUENCE IN RC WITH FULL AND LOCAL SHEAR ANISOTROPY

Amorn PIMANMAS[1] and Koichi MAEKAWA[2]

[1] Member of JSCE, Ph.D., Research fellow, Dept. of Civil Eng., The University of Tokyo
(Hongo 7-3-1, Bunkyo-ku, Tokyo 113, Japan)
[2] Member of JSCE, Dr. of Eng., Professor, Dept. of Civil Eng., The University of Tokyo
(Hongo 7-3-1, Bunkyo-ku, Tokyo 113, Japan)

An artificial crack device (ACD) is recently proposed to control crack localization. Behaviors of ACD-embedded beams, especially failure path formation and crack sequence, are complicated, due to the local shear anisotropy at ACD interface. Finite element analysis is used to analyze the problem. Fixed crack model with full degree of freedom in describing kinematics of the cracked element is employed because of the independence of principal stress and strain vectors. Explicit treatment of mode I softening and mode II aggregate interlock allows realistic crack behavior. Through the minimum potential energy in FEM, failure path of beam with shear anisotropy is simulated.

Key Words : *artificial crack device, anisotropy interaction, local shear anisotropy, fixed crack approach, failure path formation*

1. INTRODUCTION

Artificial Crack Device[1] (ACD) has been recently proposed by the authors for two purposes. The first is to decrease the quantity of shear reinforcements, and the second is to control the crack localization. Both objectives may be useful for the RC design and construction. The reduction in the usage of shear reinforcements may benefit the construction and quality of hardened concrete. The control of crack localization encourages engineers to manage the crack propagation behavior in RC members. The control of crack localization may lead to the effective usage of shear reinforcements in the conventional RC design method.

Shear tests on ACD-embedded beams have shown the possibility of all basic crack controls[1]. When ACD is inclined orthogonal to the direction of diagonal crack propagation, up to 50% increase in loading capacity is obtained. In this paper, the authors aim at simulating the behavior of ACD-embedded beams. It is noted that the formation of failure path in ACD-embedded beam is quite complicated. The increase in loading capacity is due to the mechanism of crack arrest and diversion[2]. This cannot be easily analytically reproduced.

The finite element analysis is used to simulate the formation of failure path in pre-cracked reinforced concrete beams[3),4)]. Based upon the principle of the minimum potential energy, it is verified that the finite element analysis can reproduce the failure path of pre-cracked beams successfully. However, the pre-cracked beam problem represents full shear anisotropy since pre-cracks penetrate the entire sections of the beam. For ACD-embedded beams, ACD does not penetrate the entire section, thus, the local shear anisotropy is created. In this paper, the finite element analysis is conducted to investigate the ACD-embedded beam with local shear anisotropy.

2. REVIEW OF CRACK LOCALIZATION CONTROL

Based upon the crack arrest and diversion mechanism[2], *Artificial Crack Device*[1] (**Fig.1**) has recently been proposed by the authors as the means to control the crack propagation besides reinforcing bars. Basic controls of crack localization consist of (1) specification of crack occurrence; (2) diversion of crack propagation; and (3) arresting crack propagation (**Fig.2**). Experiment on ACD-embedded beam has been conducted[1]. All above crack controls have been shown in the experiment (**Fig.3**). **Fig.3a** and **Fig.3b** show the specification of crack occurrence and the diversion of crack propagation, respectively. **Fig.3c** shows crack arrest mechanism, which increases the shear capacity of the member.

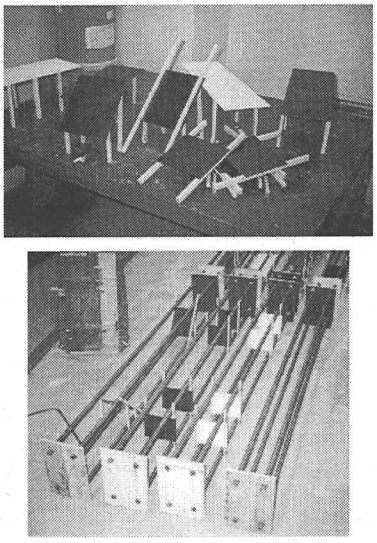

Fig.1 Artificial crack device (ACD)[1)]

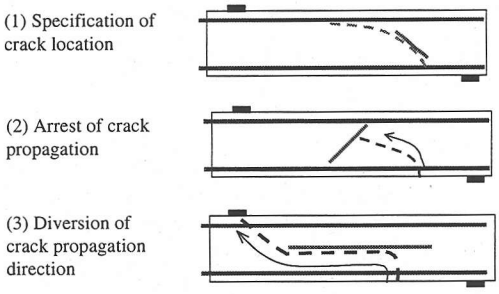

Fig.2 Basic controls of crack localization[1)]

Even if the failure crack pattern looks similar to the case of reference beam (**Fig.3c** and **Fig.3d**), the process of crack formation is different. It is observed that crack 2 in **Fig.3c** is arrested by ACD without forming the failure path successfully. The ultimate failure is caused by the independent formation of crack 3, which combines with crack 2 into a single crack and brings about failure to the beam. On the other hand, the failure in the reference beam is caused by the continuous propagation of the first diagonal crack, crack 2 into crack 3 (**Fig.3d**). The experiment on ACD-embedded beams has shown that the failure path formation can greatly affect the beam behavior. By using ACD, the failure path formation can be modified.

3. SHEAR ANISOTROPY

The common character of pre-crack and ACD is that they induce the shear anisotropy in the RC member. Under the imposed strain, enough stresses cannot be developed in concrete elements adjacent

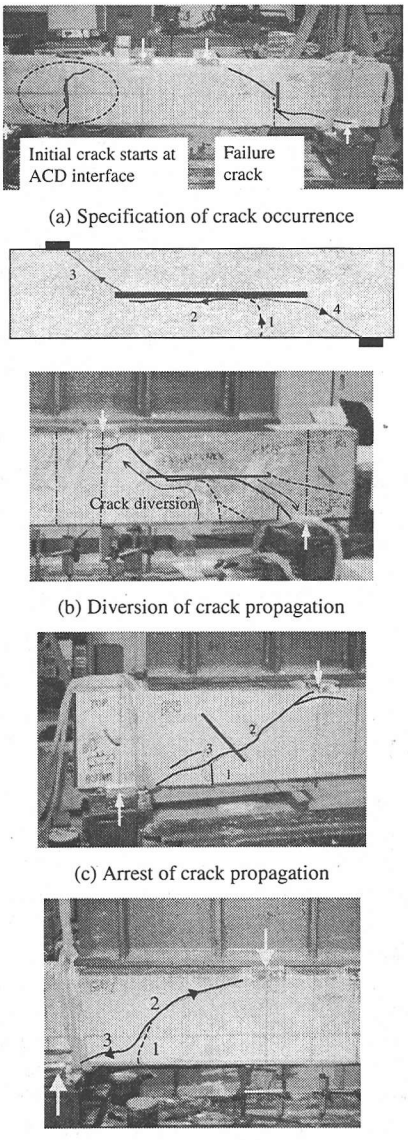

Fig. 3 Experimental realization of all basic localization controls[1)]

to ACD due to the low stress transfer ability at ACD interface. This results in crack arrest mechanism (**Fig.4**). Instead, the imposed shear strain is mainly transformed into interface slip. The terms "crack arrest and diversion" is self-explained, crack arrest means the arrest of diagonal crack whereas crack diversion means the slip at the interface (**Fig.4**). All experimental results of shear tests on pre-cracked beams[2)] and ACD-embedded beams[1)] can be consistently explained by the concept of shear anisotropy.

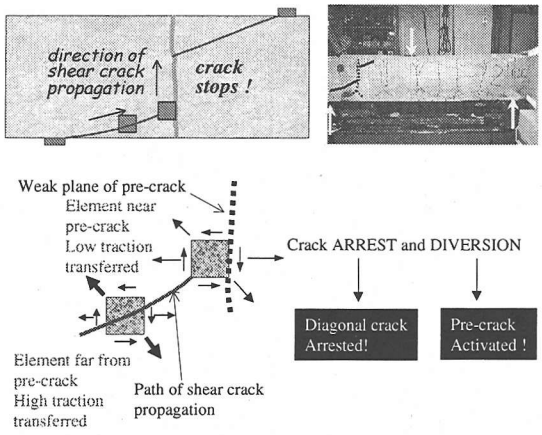

Fig.4 Mechanism of crack arrest and diversion[2)]

4. FOUR-WAY FIXED CRACK MODEL

It is shown in previous experiment[1),2)] that the shear anisotropy affects the failure path formation and the crack propagation behavior. Due to the shear anisotropy, principal stress vector will not coincide with principal strain vector. Consequently, the shear behavior is independent from normal action. In order to reproduce this behavior, the crack model has to explicitly consider the shear transfer model along ACD and pre-crack interface.

It was pointed out before[3),4)] that the rotating crack approach[5)-8)] assumes the co-axiality between principal stress and principal strain vectors, thus, it is not applicable for problem with shear anisotropy. On the contrary, the fixed crack approach explicitly considers Mode I normal crack stress release and Mode II shear traction transfer. For the 2-D finite element, the fixed crack approach considers maximum degree of freedom of the element. This allows the independent treatment of shear and normal actions (**Fig.5**), which is the basic requirement of the anisotropy.

In a 2-D finite element, kinematic variables include tensile strain normal to a crack, compressive strain parallel to a crack and shear strain along crack interface. Corresponding static variables include tensile stress normal to a crack, compressive stress parallel to a crack and shear stress along crack interface. The relationships between kinematic and static variables are described by constitutive equations.

The treatment of full degree of freedom in describing the kinematics of cracked element is necessary for the simulation of the failure path and crack sequence. FEM is supposed to reproduce the formation of failure path due to the principle of the minimum potential energy. The potential energy of

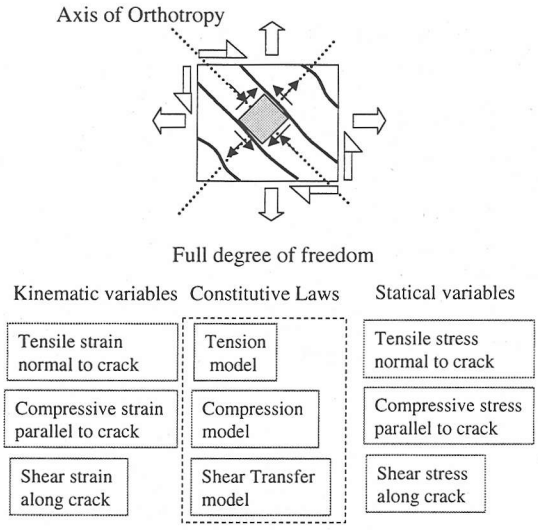

Fig.5 Scheme of fixed crack approach

the member can be minimized if the maximum degree of freedom of the element is considered.

One of the recent developments in line with the fixed crack scheme is the multi-directional four-way fixed crack approach proposed by Fukuura and Maekawa[9),10)]. This crack scheme was installed in the WCOMD[11)] general nonlinear path-dependent finite element analysis program, which is used for the numerical analysis in this paper. Four-way fixed crack model can be regarded as the generalization of two-way cracking approach[11)], implemented such that up to four cracks in arbitrary orientations at any Gauss point can be covered. The active crack scheme is preserved but the applicability has been extended to the co-ordinate level.

In the scheme of four-way cracking concept, a maximum of two orthogonal co-ordinates can be established at an integration point of the element. In each co-ordinate, at most 2 cracks are allowed. Two cracks associated with a co-ordinate system need not be perfectly orthogonal but must satisfy the quasi-orthogonal condition that the angle between them is larger than 67.5° but less than 112.5°. Upon the generation of the first crack, the first co-ordinate system is established. If the next crack is generated and meets the aforementioned angular criterion, it will be treated by the same co-ordinate, otherwise, the second co-ordinate is set-up. The assignments of the co-ordinate systems and the generation of new cracks will be implemented according to this rule until up to four-way cracks are induced at a Gauss point of RC element.

Fig.6 describes the flow of stress computation in this scheme. The active crack concept is based on the fact that under the multi-cracking situation, overall non-linearity is generally prevailed by

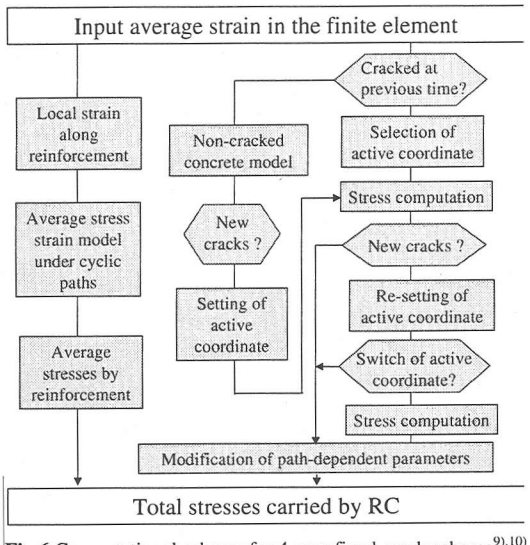

Fig.6 Computational scheme for 4-way fixed crack scheme[9),10)]

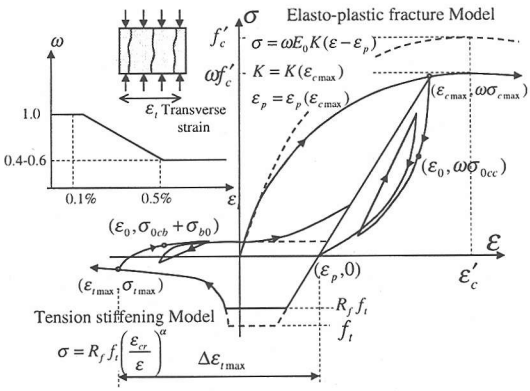

Fig.7 Coupled compression-tension model for normal stresses parallel and perpendicular to a crack[9),10)]

certain cracks while others are hardly activated. In each co-ordinate, the crack of which normal strain is smaller is considered dormant due to its higher stiffness. In each co-ordinate, the stress computation is undertaken along the selected active crack. Then the active co-ordinate is judged by comparing the normal strain of the active crack in each co-ordinate. Eventually, the final stresses of the element are stresses of the active crack in the selected active co-ordinate. Regarding revision of path-dependent variables, since concrete stresses along normal and parallel to cracks are highly-path dependent, the update of path-dependent parameters is carried out in both active and dormant co-ordinates. However, the evolution of shear is hardly mobilized in the dormant co-ordinate, thus shear related path-dependency is not revised in the step computation.

For the RC element, the local constitutive laws are required for both concrete and reinforcement.

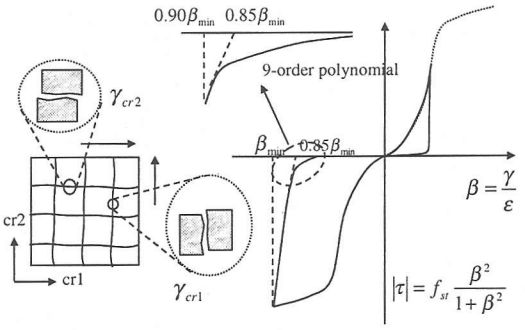

Fig.8 Shear transfer model[9),10)]

Local constitutive laws of cracked concrete are formulated along the crack axis. Local constitutive laws of reinforcing bar are formulated along the bar axis. The local distributions of stresses and strains in the cracked RC element are not uniform due to bond action at the concrete-steel interface and local traction transfer along crack interface. In the smeared crack approach, the constitutive laws are expressed in terms of average stress-average strain relations. The constitutive laws of cracked concrete consists of the tensile stress model perpendicular to the crack, the compressive stress model parallel to the crack and the shear transfer model along crack.

The coupled compression-tension model is adopted for computing normal stresses perpendicular and parallel to the crack axis (**Fig.7**). The concrete tensile stress perpendicular to the crack axis is described by the coupled tension stiffening and bridging softening relationship in line with the zoning approach[12)]. In the model, concrete near reinforcements is assumed to have gradual stress release after cracking due to tension stiffening effect (RC zone). In contrast, concrete far from reinforcement follows the plain concrete behavior (PL zone) with sharp stress release due to bridging softening at the crack interface. In compression, the elasto-plastic fracture model[11)] is used to compute compressive stress parallel to the crack axis. The model combines the non-linearity of plasticity and fracturing damages to account for the permanent deformation and loss of elastic strain energy capacity, respectively. The effect of orthogonal tensile strain in reducing the compressive stress transfer is also taken into account[13)].

To model shear transfer along the crack interface, the shear transfer model based upon the contact density theory[14)] is adopted (**Fig.8**). In the multi-cracking situation, the total imposed shear strain is decomposed into the shear strain due to cracks and shear strain due to un-cracked concrete. Hence, the computation of the overall shear modulus of the cracked element must consider the

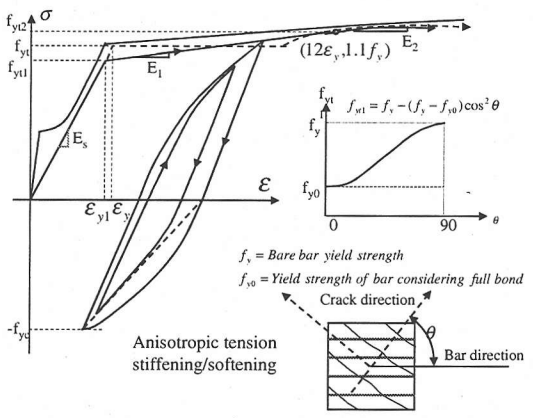

Fig. 9 Modeling of reinforcing bar[9),10)]

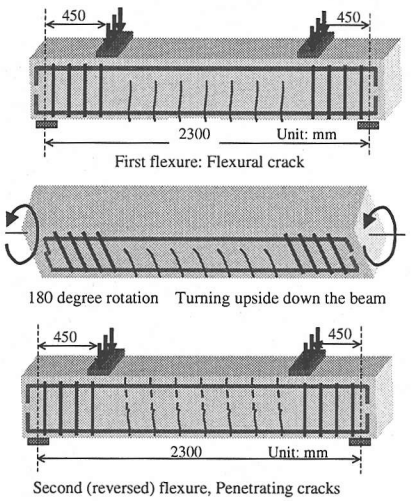

(a) First step-reversed flexural loading

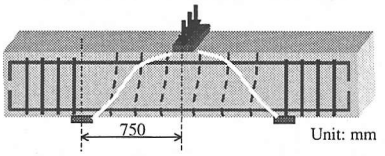

(b) Second step-shear loading

Fig.10 Experimental outline of shear test on pre-cracked beam[2)]

contribution of the concrete between cracks and each crack in the active crack co-ordinate[9),10)].

The model of reinforcing bars (**Fig.9**) considers the effect of localized plasticity[15)] at the vicinity of crack planes. The reduced yield strength due to bond transfer between concrete and steel bar is taken into account. Since cracks in reinforced concrete element need not be orthogonal to the reinforcement direction, the bond effect is not fully effective in such case. Reinforcing bar orthogonal to crack is supposed to have full bond effect. On the contrary, reinforcing bar parallel to crack is supposed to show uniform stress profile like bare bar rods in tension. Then, the computation of mean yield strength has to take into account the angular deviation of normal to crack from reinforcing bar direction[16)]. These local constitutive laws were reformulated and detailed by Fukuura and Maekawa[9),10)].

5. VERIFICATION OF MULTI-DIRECTIONAL FIXED APPROACH FOR FULL ANISOTROPY PROBLEM

The shear test on pre-cracked beam[2)] represents the RC problem with full anisotropy since pre-cracks penetrate the entire sections[2)-4)]. The full discussion of the experimental results[2)] and the numerical analysis are reported earlier[3),4)]. Here, the authors briefly address them to show that the four-way fixed crack model[9),10)] can simulate the problem with full shear anisotropy. Experimental outline[2)] is shown in **Fig10**. Pre-cracks were introduced into the beam by means of reversed flexural loading (**Fig.10a**). To conduct shear test, supports were moved towards beam mid-span **Fig.10b** such that the ratio of shear span to effective depth was 2.41. The shear loading caused diagonal crack to propagate across pre-crack planes.

The dimension and cross section of the beam are shown in **Fig.11a**. Tested average compressive strength of concrete is 26.5 MPa. Tested yield strength of main and shear reinforcements is 338.4 MPa. Two cases are considered; one uses only smeared elements and the other uses both smeared and discrete joint elements to represent pre-cracks. The finite element meshes of these two cases are shown respectively in **Fig.11b** and **Fig.11c**. These two analyses are referred respectively as the smeared case and the smeared-discrete case.

Load-displacement relationships under shear loading are shown in **Fig.12**. As shown in the figure, the behavior of pre-cracked beam significantly differs from the non pre-cracked one. Pre-cracked beam reaches much higher loading capacity, displacement ductility and energy consumption, but with much lower initial stiffness. Basically, both cases, i.e., smeared and smeared-discrete cases, can predict loading capacity and load-displacement relation throughout the entire loading curve.

As can be observed from the figure, numerical load-displacement curves are not smooth but show the serrated pattern instead. Experimental curves also show this characteristics which is due to the crack arrest and diversion mechanism[2)]. Once the diagonal crack is formed, load drops. However, since diagonal crack cannot propagate continuously across pre-crack planes, higher load can be resisted.

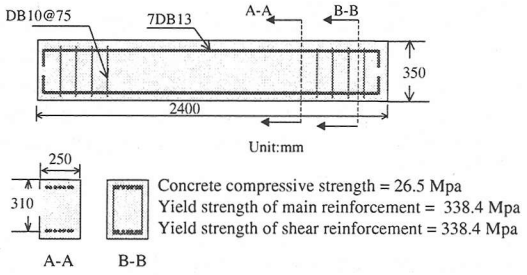

(a) Dimension and cross section of beam[2-4)]

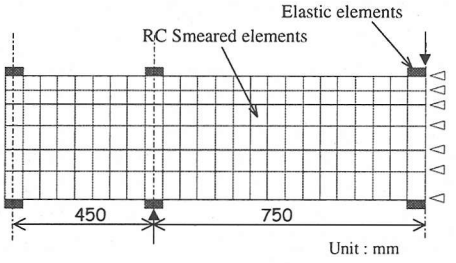

(b) FEM mesh: Only smeared elements used

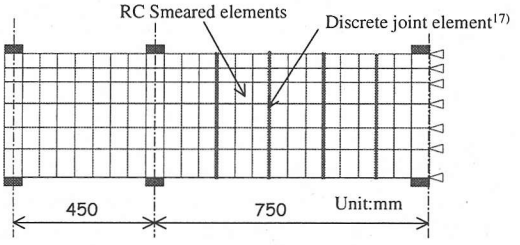

(c) FEM mesh: Smeared + discrete joint elements[17)]

Fig.11 Dimensions, cross section, material properties and FEM mesh of pre-cracked beam problem[2)]

This explains periodic cycles of temporary drop and increase in load-displacement curves. However, the smeared case seems to predict higher irregularity than the experiment. This is possibly due to the deficiency of smeared element of larger sizes in simulating discrete crack.

The crack patterns during the initial stage of both cases are shown in **Fig.13**. The thickness of numerical crack lines indicates the tensile strain level normal to the crack. For example, bold crack lines mean higher tensile strain than thin crack lines. However, these crack lines do not necessarily coincide with real cracks because in a smeared element, cracks are predicted at Guass points only. Both smeared and smeared-discrete cases can predict Z-cracks[2)] around each pre-crack similar to the experiment. Final failure crack patterns of both two cases are compared in **Fig.14**. To aid the visualization, two crack patterns corresponding to main and secondary failure cracks are separately drawn. It is seen that FEM can capture both crack

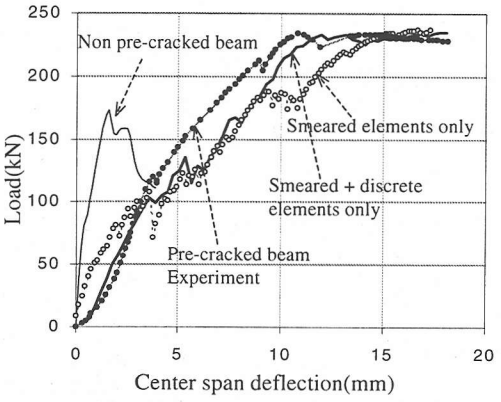

Fig.12 Comparison of numerical and experimental results[2),3)]

(a) Z-cracks captured in the smeared case

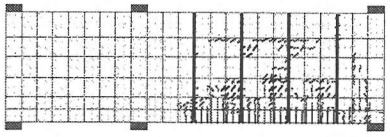

(b) Z-cracks captured in the smeared-discrete case

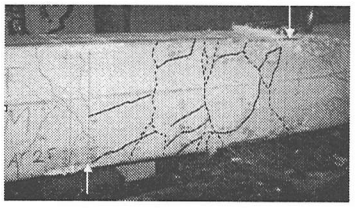

(c) Z-cracks in the experiment

Fig.13 Comparison of crack pattern during initial loading stage

paths consistently. The disconnected pattern of the main failure crack verifies that FEM can simulate the independent development of cracks and subsequent combination of them. Thus, the ability of FEM in simulating the failure path of the problem with full shear anisotropy is verified.

6. SIMULATION OF FAILURE PATH FORMATION FOR RC MEMBERS WITH LOCAL SHEAR ANISOTROPY

In this section, the ACD-embedded beam representing the local shear anisotropy is numerically investigated. It is noted that the failure path formation in ACD-embedded beam is variously

Secondary cracks captured by FEM

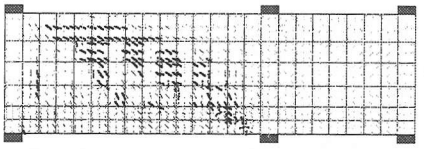

Main failure cracks captured by FEM

(a) Smeared case

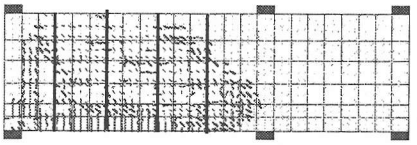

Secondary cracks captured by FEM

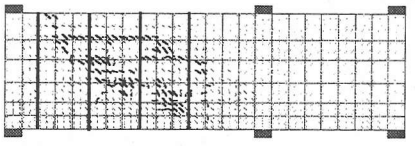

Main failure cracks captured by FEM

(b) Smeared + discrete case

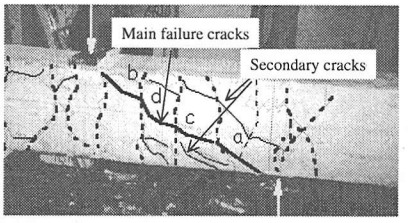

(c) Experimental failure crack pattern

Fig.14 Comparison of failure crack pattern

depending upon the arrangement of ACD inside the member[1]. First, the failure process in the ordinary slender beam due to the unstable propagation of a single diagonal crack is simulated. This is considered as the conventional shear failure, which represents the shear isotropy case.

(1) Failure path formation in ordinary slender beam

The FEM mesh used is shown in **Fig.15** together with the beam cross section. Reinforcement ratio is 1.548 %. The shear span to effective depth ratio is 2.8. Assumed compressive strength of concrete is 31.4 MPa. Assumed yield strength of main bar is

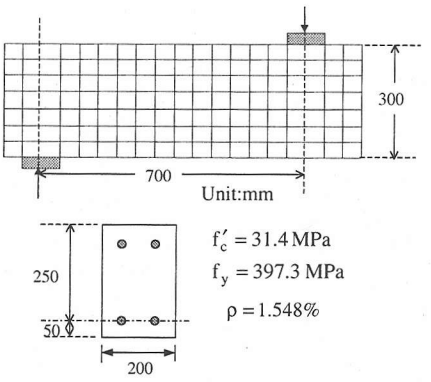

Fig. 15 Finite element mesh, material property and cross section

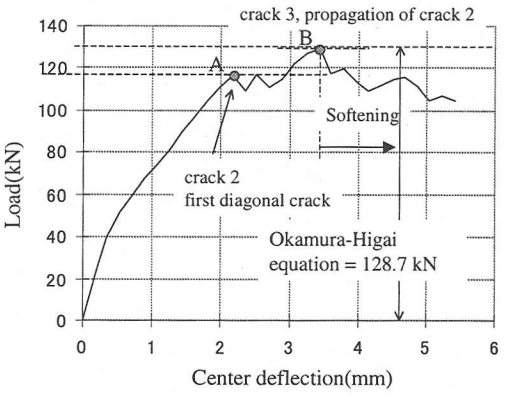

Fig.16 Numerical load-displacement relationship

397.3 MPa. Load-displacement relationship is shown in **Fig.16**. The sequence of crack formation in the experiment is described in **Fig.17a**. The sequence of failure path captured by FEM is shown in **Fig.17b**. FEM captures the first diagonal crack at the web zone of the beam at the load 115.2 kN (point A in the load-displacement relation). FEM subsequently predicts the propagation of this diagonal crack in the following steps but without drop in load. Applied load keeps increasing up to point B at which a flatter diagonal crack equivalent to crack 3′ (**Fig.17a**) is formed which leads to the failure and drop in loading capacity. The numerical simulation of the crack sequence closely follows the experimental observation.

In the experiment, the sudden formation of crack 4 (**Fig.17a**) may be observed with the explosive sound and the corresponding sharp drop in the loading capacity. Crack 4 normally propagates through the end of the beam despite the fact that no stresses can be transferred. The sudden formation of crack 4 indicates the abrupt release of energy out of the beam. As shown in **Fig.17c**, the analysis can also reproduce crack 4.

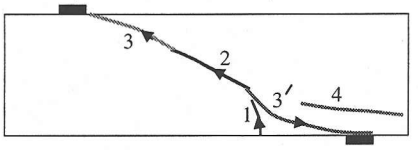

Crack 1: Flexural crack
Crack 2: Advent of first diagonal crack
Crack 3,3': Propagation of crack 2
Crack 4: Sudden energy release from the beam

(a) Experimental failure process in an ordinary slender beam

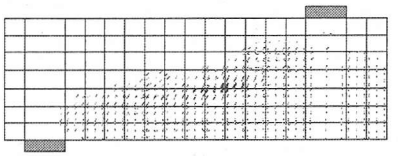

A : P = 115.2 kN, crack 2 appears

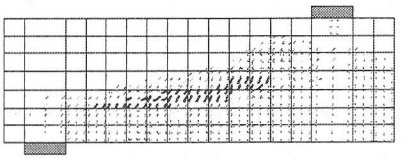

Just before B (formation of crack 3′)
P = 129.7 kN

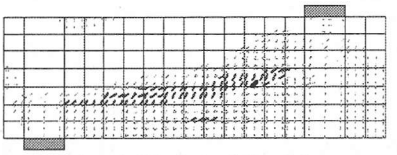

At B (crack 3′is formed) Load drops
P = 117.6 kN

(b) Sequence of failure path captured by FEM

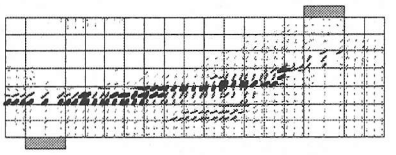

(c) Experiment and numerical formation of crack 4 penetrating horizontally towards the beam end

Fig.17 Numerical failure path formation in ordinary slender beam

(2) Simulation of failure path formation in ACD-embedded beam with local shear anisotropy

Shear tests on seven ACD-embedded beams[1)] are numerically investigated in this section. Beam 1 is the reference beam without ACD inside. The rest

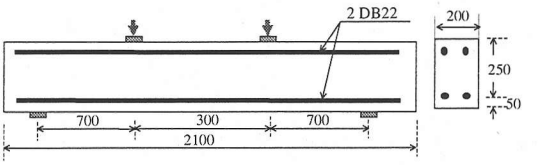

Fig.18 Loading arrangement

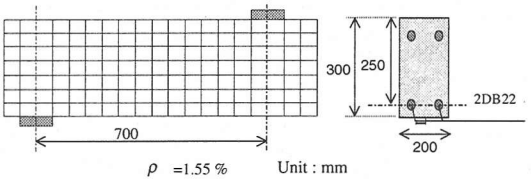

Fig.19 Finite element mesh of the non ACD-embedded beam 1

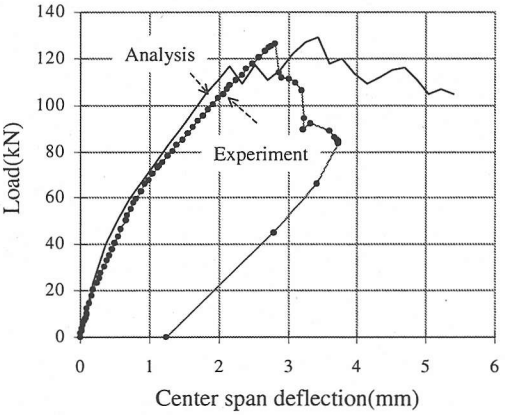

(a) Load-displacement relationship of beam 1(No ACD) (Numerical and experimental result)

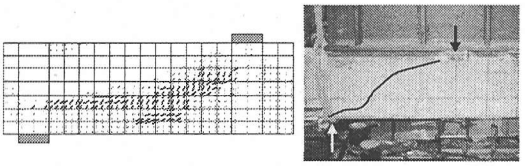

(b) Numerical and experimental failure crack pattern

Fig.20 Comparison of numerical and experimental result of beam 1(Non ACD-embedded beam)

six beams are embedded with ACD in various arrangements. Main reinforcement ratio is 1.55%. No shear reinforcements are provided inside the beams. Tested yield strength of reinforcing bars is 397.3 MPa. Tested concrete compressive strength is 31.4 MPa. Loading arrangement is shown in **Fig.18**. The shear span to effective depth ratio is 2.8. The shear capacity predicted by Okamura-Higai Equation is 64.35 kN. The flexural capacity predicted by the sectional theory is 69.9 kN-m. Therefore, load corresponding to shear capacity (P_v) and flexural capacity (P_y) is respectively 128.7 kN and 199.7 kN.

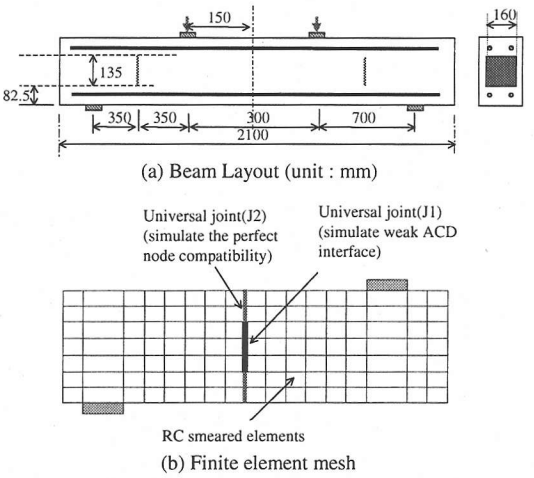

Fig.21 Layout and finite element for ACD-embedded beam 2

a) Numerical analysis of beam 1 (reference beam without ACD)

Finite element mesh is shown in **Fig.19**. Due to symmetry, the analysis of only half beam is sufficient. Comparison of the experimental and numerical load-displacement relationships is shown in **Fig.20a**. Close agreement is obtained in the pre-diagonal crack behavior. However, the softening path does not match well with the experimental result. It is noted that the softening behavior depends on the coupled deformation of cracks in mode I and mode II. Currently, the correct shear softening model is not available. More research in this area is needed.

Numerical crack pattern is shown in **Fig.20b** compared with experimental result. The localization of crack can be simulated. The successful prediction of crack propagation is due to the installation of mode I softening normal stress release in line with the zoning concept[12], which allows the treatment of fracture mechanics in FEM.

b) Numerical analysis of ACD-embedded beam 2

In beam 2, a steel ACD is arranged vertically at the center of shear span in each side of the beam as shown in **Fig.21a**. Finite element mesh is shown in **Fig.21b**. To model the smooth interface at the concrete-ACD contact, interfacial joint element is used. Since the exact constitutive properties of ACD-concrete interface are not available, the constitutive properties of the joint element in both tangential and normal directions are assumed as shown in **Fig.22**. The normal stiffness is assigned very low value in tension but very high value in compression. The shear stiffness is assigned very low value in both tension and compression. This joint property is referred to as J1 in the mesh.

At the location of ACD in the mesh, the joint elements are inserted throughout the entire section.

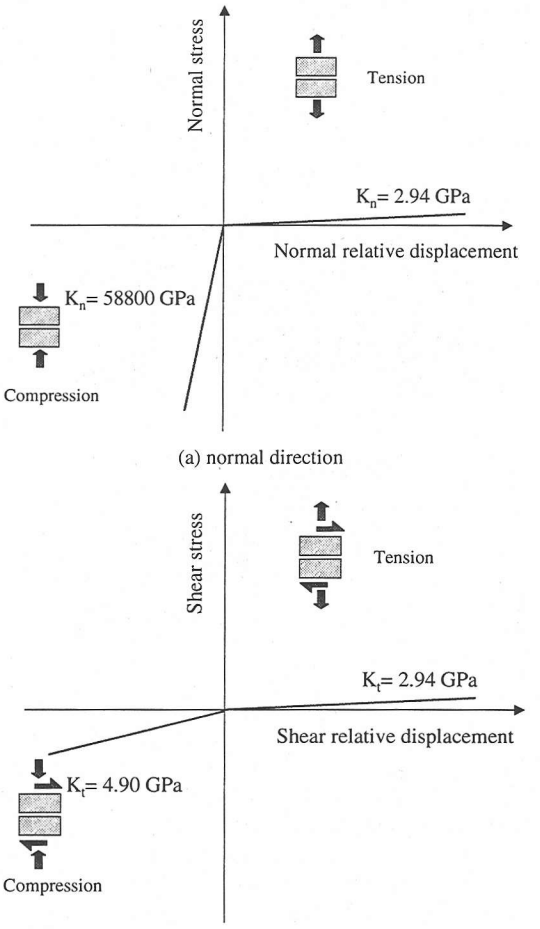

Fig.22 Constitutive properties of interfacial joint element representing ACD-concrete interface

This is necessary since the insertion of interfacial elements add extra nodes. If interfacial elements are only installed at the partial portion of the section, then the FEM connectivity with adjacent elements is not consistent. Here, for representing the locally different connectivity along the cross section correctly (**Fig21b**), different constitutive properties are given to the inserted joint elements. For ACD interface portion, joint J1 is used. For continuum concrete above and beneath the ACD, a joint J2 with very high shear and normal stiffness are assumed. J2 joint is computationally equivalent to the perfect compatibility of monolithic concrete. These assumed interfacial joint properties are maintained for all subsequent beam analyses.

The analysis predicts initial cracks forming around ACD as shown in **Fig.23** (Top), which is similar to the experiment. This means that the analysis recognizes the local shear anisotropy at the

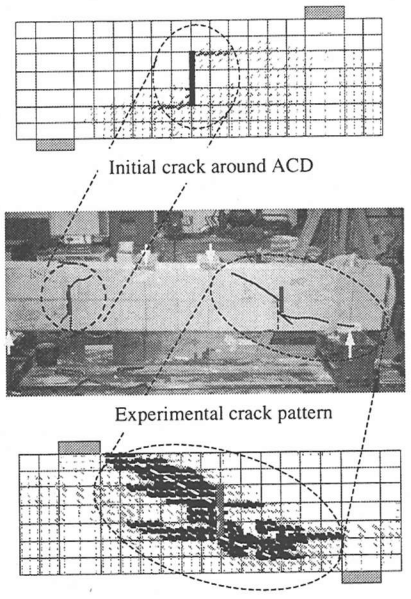

Fig.23 Numerical and experimental crack pattern for ACD-embedded beam 2

ACD interface, which can transfer only small shear stress. Hence, no stress concentration can be developed diagonally at the ACD interface, and therefore no formation of diagonal cracks. However, at the top and bottom ends of ACD, full shear transfer is provided, thus allowing the generation of diagonal cracks there.

Now the failure formation is investigated. Further loading predicts the propagation of the aforementioned initial cracks towards loading point on one side and backwards support on the other side. The crack propagation and the final failure crack pattern are similar to the experimental observation as shown in **Fig.23** (Middle and bottom). No propagation of cracks across the ACD is predicted. The propagation of diagonal cracks avoiding the ACD can be numerically reproduced. The comparison of numerical and experimental load-displacement relationships is shown in **Fig.24**. Close agreement can be obtained up to the peak load. However, post peak softening is not accurately predicted.

c) Numerical analysis of ACD-embedded beams 3 and 4

In beam 3 and beam 4, two vertical ACD were provided in each shear span of the beam as shown in **Fig.25a**. In the experiment, steel ACD is used in beam 3 whereas plastic ACD is used in beam4. Experiment showed no difference between steel and plastic ACD. It is supposed that the strength of ACD does not affect the crack propagation. The effect of

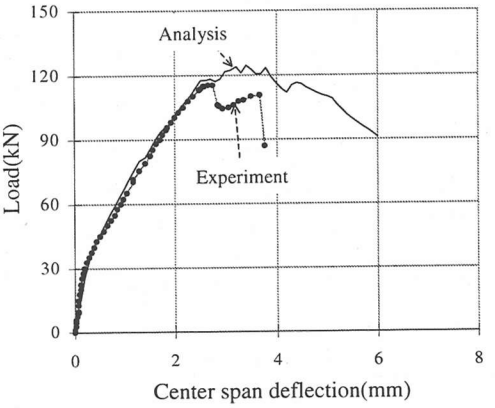

Fig.24 Load-displacement relationship of ACD-embedded beam 2 (Numerical and experimental results)

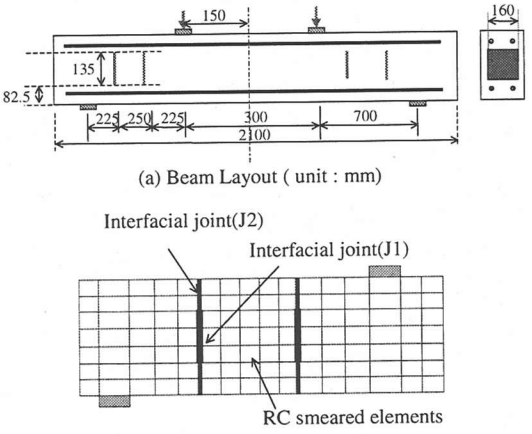

Fig.25 Layout and finite element mesh of ACD-embedded beams 3,4

stiffness is not clarified in the experiment. It is considered that the smooth interface is the main factor for the shear anisotropy. Thus the difference between stiffness of plastic and steel is not considered in the analysis of beam 3 and beam 4. However, the experimental failure path in beam 3 and beam 4 is a little bit different regarding the location of the central diagonal crack as shown in **Fig.30**. It is interesting to know the shape of failure path selected in the analysis.

Finite element mesh is shown in **Fig.25b**. Two rows of interfacial joint elements with low shear stiffness are employed to represent two embedded ACD. Initial crack pattern simulated in the analysis is shown in **Fig.26**. Similar to beam 2, the analysis predicts two fairly flat diagonal cracks initially formed at the top and bottom ends of each ACD in the similar way as the experiment.

The comparison of numerical and experimental

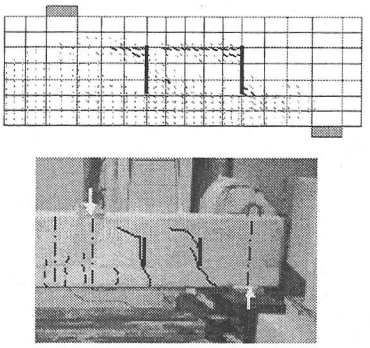

Fig.26 Initial cracks form around ACD in ACD-embedded beams 3 and 4

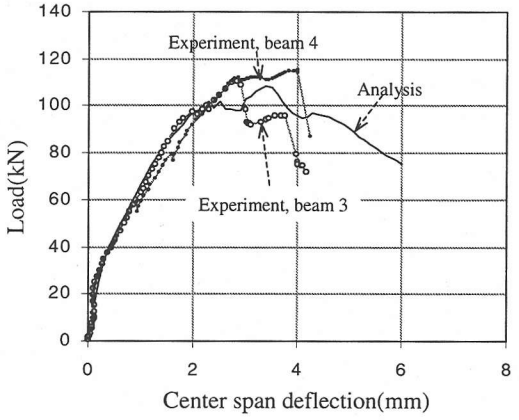

Fig.27 Load-displacement relationship of ACD-embedded beams 3, 4 (Numerical and experimental results)

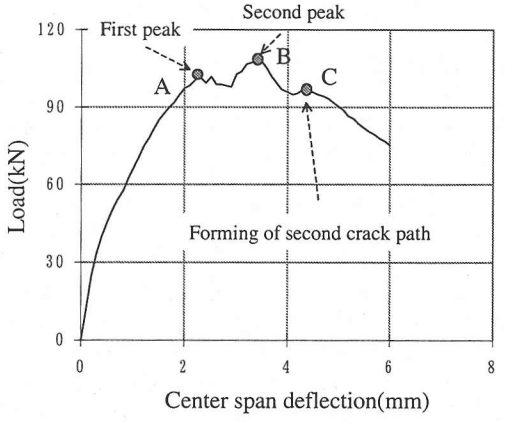

Fig.28 Examination of numerical load-displacement relationship for ACD-embedded beams 3, 4

load-displacement relationships is shown in **Fig.27**. The analysis agrees closely with the experimental result in the pre-peak range. It is noticed that two peaks exist on the numerical load-displacement curve. The crack pattern corresponding to these two peaks is examined. In **Fig.28**, only the numerical

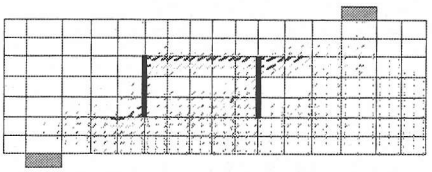

(a)Crack pattern at peak 1
extension of initial crack around ACD

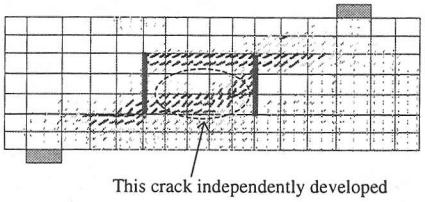

(b) Crack pattern at peak 2
development of new independent diagonal crack between ACDs

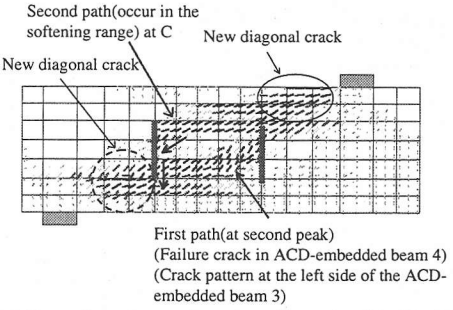

(c) Formation of second crack path at point C in **Fig.28**

Fig.29 Crack formation sequence in ACD-embedded beams 3, 4

load-displacement relationship is shown. The crack pattern at the first peak is shown in **Fig.29a**. As shown in the figure, this crack is the small extension of initially formed diagonal crack around each ACD. No continuous failure path is yet constructed, therefore, the beam keeps on resisting the applied load. At the second peak or ultimate load, new diagonal crack is independently developed between the beam portion bounded by two ACDs as shown in **Fig.29b**. The formation of this crack then completes the failure path for transferring the force from loading point to support and results in the ultimate failure. This computed crack pattern resembles the failure crack in the experiment of beam 4 and can also be seen in the left side of beam 3 as shown in **Fig.30b** and **Fig.30a**, respectively.

The development of the failure path in this way is not affected by the presence of ACD. On the contrary, initially formed diagonal crack around ACD helps facilitating the failure since it readily combines with the aforementioned independently formed diagonal crack. Similar to the experiment,

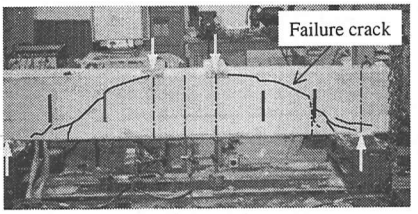

(a) Experimental failure crack in ACD-embedded beam3

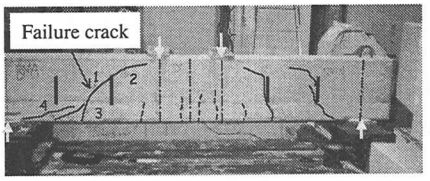

(b) Experimental failure crack in ACD-embedded beam 4

Fig. 30 Failure crack pattern in ACD-embedded beams 3, 4

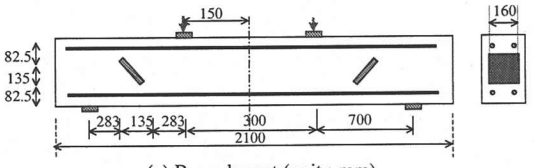

(a) Beam layout (unit : mm)

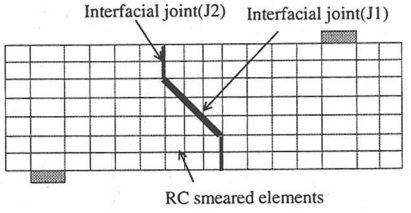

(b) Finite element mesh

Fig.31 Layout and finite element mesh of ACD-embedded beam 5

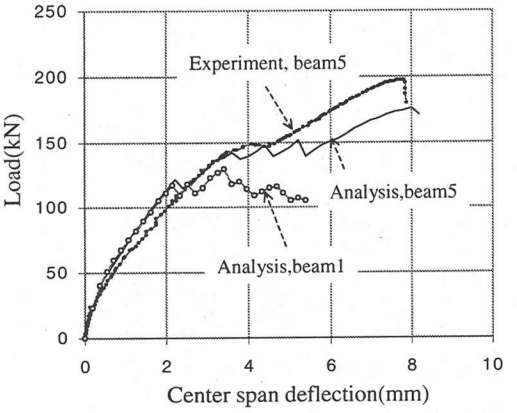

(a) Comparison of load-displacement relation of beam 5

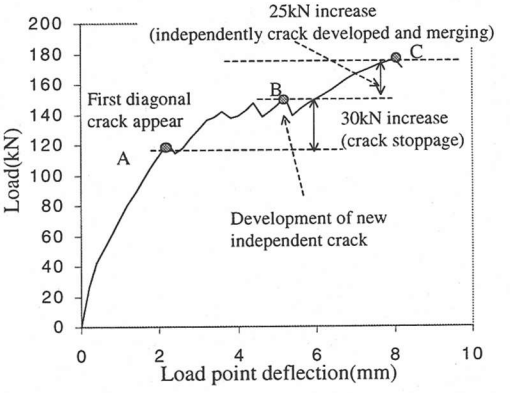

(b) Numerical load-displacement relationship of beam 5

Fig.32 Load-displacement relation of beam 5

the analysis does not predict the crack arrest and diversion phenomenon.

The crack formation on the softening path of the load displacement curve is now investigated. As reported, the shape of failure path in beam 3 is a little different from beam 4. As loading progresses, it is seen that the diagonal crack at the top of the left ACD becomes active and starts propagating backward as shown in **Fig.29c**. The propagation then diverts its direction into along the ACD interface without penetrating through the ACD. This crack finally joins with the initially existing diagonal crack at the bottom of ACD. As a result, the formed crack attains the shape similar to the failure crack in beam 3. Here, it is seen that FEM can simulate the failure path similar to both beam 3 and beam 4

d) Numerical analysis of ACD-embedded beam 5

In beam 5, the steel ACD is inclined orthogonal to the diagonal shear crack (**Fig.31a**). Experiment has shown that such inclination is effective in arresting the crack propagation and greatly increasing the beam capacity. Finite element mesh is shown in **Fig.31b**. Comparison of numerical and experimental load-displacement relationships is shown in **Fig.32a**. In **Fig.32b**, only the numerical load-displacement relationship of beam 5 is shown to trace the process of crack formation.

The sequence of crack formation is shown in **Fig.33**. Initial cracks (**Fig.33a**) are formed at the load around 121 kN (point A in **Fig.32b**). The crack is developed at the web portion at the right side of ACD. This crack tries to propagate downward support but is not successful due to the presence of ACD. The crack arrest is simulated in the analysis. It is seen than the computed crack becomes widening locally without further propagation (**Fig.33b**). The crack arrest mechanism remains effective until at point B, where a new diagonal crack is independently formed (**Fig.33c**). The load increase from point A to point B is 30 kN or 23% of the shear capacity of reference beam.

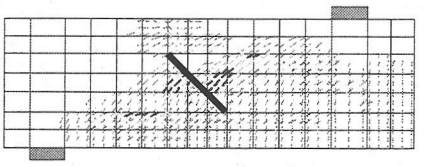

(a) Arrival of the first diagonal crack

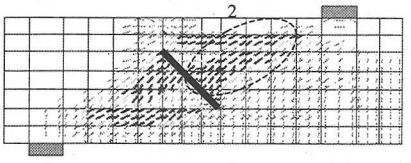

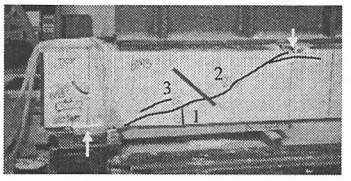

(b) Crack arrest phenomenon

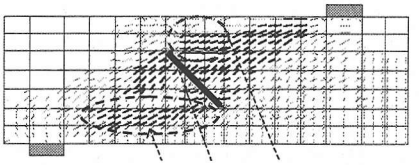

Newly developed crack, crack 3

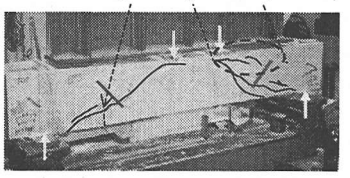

c) Newly developed crack 3

Fig.33 Sequence of crack formation in ACD-embedded beam5

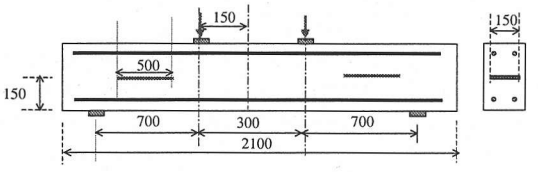

(a) Beam Layout (unit : mm)

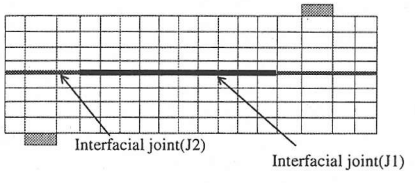

(b) Finite element mesh

Fig.34 Layout and finite element mesh of ACD-embedded beams 6, 7

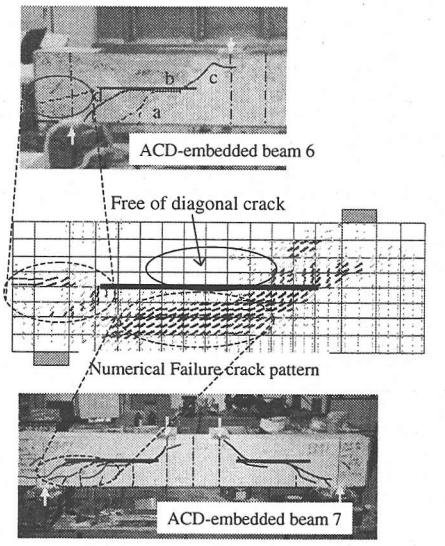

Fig.35 Numerical and experimental crack pattern of ACD-embedded beams 6,7

Comparison of numerical load-displacement relationship of reference beam and beam 5 is shown in **Fig.32a**. It is noted that numerical load-displacement curves of them match each other in the initial loading range, which verifies that the arrangement of ACD in this inclination does not decrease the stiffness in the pre-diagonal crack behavior.

Now, the failure path formation is investigated. The newly developed crack at point B becomes active and propagates upwards and combines with the arrested crack at point C, which indicates the completion of the failure path. During this process, load can increase up to 25 kN or 19%. Through crack arrest mechanism and formation of failure path, i.e., from the first diagonal crack at A to the completion of failure path at C, the analysis totally predicts 55 kN or 42% increase in loading capacity compared to 56% increase in the experiment. It is seen that FEM underestimates the increase in loading capacity.

e) Numerical analysis of ACD-embedded beams 6 and 7

In beams 6 and 7, one horizontal ACD is installed at the centroidal axis in each side of shear span as shown in **Fig.34a**. In beam 6, steel ACD is used while in beam 7, plastic ACD is used. Finite element mesh is shown in **Fig.34b**. The numerical crack pattern is shown in **Fig.35**. Fair agreement with the experiment can be noticed. The analysis predicts neither diagonal cracks above nor across the ACD. Instead, due to the local shear anisotropy at the ACD, diversion of diagonal cracks is resulted.

Comparison of numerical and experimental load-displacement relationships is shown in **Fig.36**.

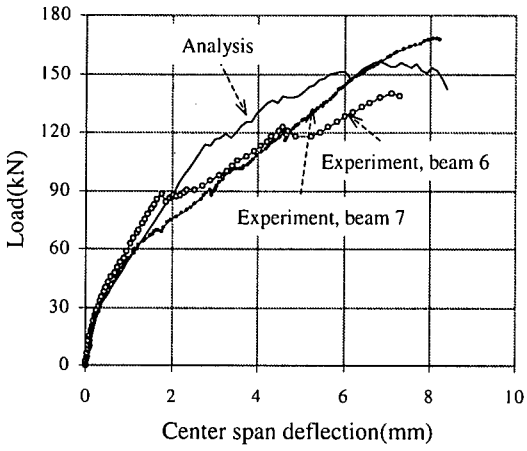

Fig.36 Load-displacement relationship of ACD-embedded beams 6, 7

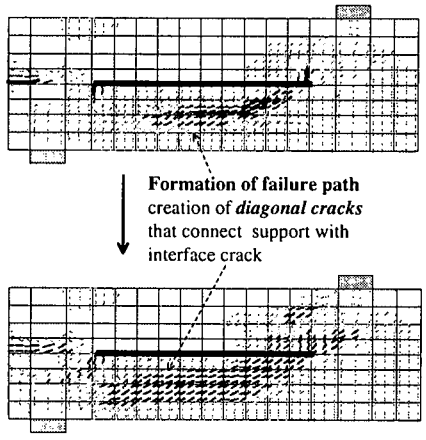

Fig.37 Formation of failure path in ACD-embedded beams 6, 7

Loading capacity can be reasonably predicted but the point where stiffness noticeably decreases in the load-displacement relation is overestimated. In the experiment, this stiffness change is due to the interface crack along ACD. Thus, in the experiment, two points where stiffness decreases are identified. The first point corresponds to the formation of flexural crack and the second point corresponds to the formation of the interface crack. However, in the analysis, the interfacial joint elements are used to represent the ACD interface. Since the constitutive laws of these joint elements are assumed linearly elastic, FEM cannot capture the immediate occurrence of the interface crack as in the experiment. As described in the experiment, the formation of the interface cracks does not cause the failure yet. Load can continue increasing while more diagonal cracks are generated. This results in the gradual reduction in stiffness as loading progresses.

In the analysis, however, the second noticeable decrease in stiffness is observed when diagonal cracks below the ACD are formed (**Fig.35, Fig.37**). Similar to the experiment, the analysis predicts the further increase in loading capacity. As load increases, the analysis predicts more cracks, which result in the gradual decrease of stiffness. The numerical crack pattern therefore shows several diagonal cracks below ACD, which is similar to the experimental observation (**Fig.35**).

Regarding the failure process, the experimental observation indicates that beams 6 and 7 fail after the diagonal crack connecting the interface crack to the support is formed (crack d in **Fig.35** Top). It is noted that the failure path is defined by the crack c-b-d. Initially formed crack a-b-c does not cause failure yet. The analysis can also reproduce this experimental observation. This is shown in **Fig.37**. Moreover, some cracks penetrating to the beam end as shown in **Fig.35** (Top, Middle) are also captured in the analysis.

7. CONCLUSIONS

For investigating the shear failure-path formation in RC beams with embedded artificial discontinuity devises, 2D nonlinear numerical analyses were conducted and the multi-directional fixed crack modeling of RC kinematics was examined. The followings are concluded as,

(1) The mechanism of increased shear capacity of RC beams with pre-embedded discontinuity, denoted by ACD in this paper, is explained with truncated diagonal cracks and enforced dispersion of secondary cracking around ACD.

(2) The combination of joint discrete interface and smeared crack modeling of multi-directional fixed crack approach can work as the simulator for failure of RC beams with metallic or non-metallic sheets that causes artificial shear anisotropy.

(3) The interaction of ACD and concrete interface can simply be idealized as joint planes with no shear stress but full contact compression transfer and free separation without cohesion.

ACKNOWLEDGEMENT: The authors would like to express their gratitude towards the Grant-in-aid for scientific research no. 12450174 in providing financial supports for carrying out the research.

REFERENCES

1) Pimanmas, A. and Maekawa, K.: Control of crack localization and formation of failure path in RC members containing artificial crack device, *J. Materials, Conc. Struct., Pavements, JSCE, August*, 2001.

2) Pimanmas, A. and Maekawa, K.: Influence of pre-crack on RC behavior in shear, *J. Materials, Conc. Struct., Pavements, JSCE,* No.669/V-50, pp. 277-291, 2001.
3) Pimanmas, A. and Maekawa, K: Multi-directional fixed crack approach for highly anisotropic shear behavior in pre-cracked RC members, *J. Materials, Conc. Struct., Pavements, JSCE,* No.669/V-50, pp. 293-307, 2001.
4) Pimanmas, A. and Maekawa, K.: Finite element analysis and behavior of pre-cracked reinforced concrete member in shear, *Accepted for publication in Mag.Conc.Res.,* 2001.
5) Cope, R.J., Rao, P.V., Clark, L.A. and Norris, P.: Modeling of reinforced concrete behavior for finite element analysis of bridge slabs, *Numerical Method for Nonlinear Problems 1,* Taylor C. et.al.(eds), Pineridge Press, Swansea, pp. 457-470, 1980.
6) Vecchio, F. and Collins, M.P.: The modified compression field theory for reinforced concrete elements subjected to shear, *ACI Journal,* Vol.3(4), pp. 219-231, 1986.
7) Vecchio, F.J.: Analysis of shear critical reinforced concrete beams, *ACI struct. J.,* Vol.97(1), pp.102-110, 2000.
8) Hsu, T.T.C.: ACI shear and torsion provisions for prestressed hollow girders, *ACI Struct. J.,* Vol. 94(6), pp. 787-799, 1997. (9)
9) Fukuura, N. and Maekawa, K.: Re-formulation of spatially averaged RC constitutive model with quasi-orthogonal bi-directional cracking, *J. Materials, Conc. Struct., Pavements, JSCE,* Vol.45, pp. 157-176, 1999.(in Japanese)
10) Fukuura, N. and Maekawa, K.: Spatially averaged constitutive law for RC in-plane elements with non-orthogonal cracking as far as 4-way directions, *J. Materials, Conc. Struct., Pavements, JSCE,* Vol.45, pp. 177-195, 1999. (in Japanese)
11) Okamura, H. and Maekawa, K.: *Nonlinear analysis and constitutive models of reinforced concrete,* Gihodo-Shuppan Co. Tokyo, 1991.
12) An, X. and Maekawa, K. and Okamura, H.: Numerical simulation of size effect in shear strength of RC beams, *J. Materials Conc. Struct., Pavements, JSCE,* Vol.35, No. 564, pp. 297-316, 1997.
13) Miyahara, T., Kawakami, T. and Maekawa, K.: Nonlinear behavior of cracked concrete plate element under uniaxial compression, *Concrete Library International, JSCE,* Vol. 11, pp. 306-319, 1988.
14) Li, B., Maekawa, K. and Okamura, H.: Contact density model for stress transfer across cracks in concrete, *J. Faculty of Eng. Univ. of Tokyo(B),* Vol.40, pp. 9-52, 1989.
15) Salem, H. and Maekawa, K.: Spatially averaged tensile mechanics for cracked concrete and reinforcement under highly inelastic range, *J. Mater. Conc. Struct., Pavements, JSCE,* pp. 277-293, 1999.
16) Hauke, B. and Maekawa, K.: Three-dimensional modelling of reinforced concrete with multi-directional cracking, *J. Materials, Conc. Struct., Pavements, JSCE,* Vol.45, pp. 349-368, 1999.
17) Mishima, T. and Maekawa, K.: Development of RC discrete crack model under reversed cyclic loads and verification of its applicable range, *Concrete library of JSCE,* No.20, pp. 115-126, 1992.

(Received May 15, 2000)

せん断異方性を内在するRC部材の破壊経路形成とひび割れ導入過程に関する数値解析

ピマンマス　アモン・前川　宏一

本研究は，せん断破壊を制御する一つの方策として，埋め込み型の人工亀裂を取り上げる．人工亀裂を予め埋め込んだはりの挙動は，破壊に至る経路やひび割れ発生順序の観点から複雑であり，主として人工亀裂によるせん断伝達機構の異方性に起因する．この問題に対して，応力とひずみの主方向に拘束条件を設けることなく，開口方向の引張破壊とずれを伴うせん断伝達の相互作用を考慮することが必要となる．そこで，多方向固定ひび割れモデルに基づく有限要素解析を適用した．これにより，予めせん断異方性を有するはりの破壊経路が解析可能であることを示した．